ACS NANO
Cite This: ACS Nano XXXX, XXX, XXX–XXX
www.acsnano.org

ARTICLE

Ultrafast Heat Flow in Heterostructures of Au Nanoclusters on Thin Films: Atomic Disorder Induced by Hot Electrons

Thomas Vasileiadis,*[,†] Lutz Waldecker,[†,∥] Dawn Foster,[‡] Alessandra Da Silva,[‡] Daniela Zahn,[†] Roman Bertoni,[†,⊥] Richard E. Palmer,[§] and Ralph Ernstorfer*[,†]

[†]Fritz-Haber-Institut, Faradayweg 4-6, 14195 Berlin, Germany

[‡]Nanoscale Physics Research Laboratory, School of Physics and Astronomy, University of Birmingham, Edgbaston, Birmingham B15 2TT, United Kingdom

[§]College of Engineering, Swansea University, Bay Campus, Fabian Way, Swansea SA1 8EN, United Kingdom

Supporting Information

ABSTRACT: We study the ultrafast structural dynamics, in response to electronic excitations, in heterostructures composed of size-selected Au nanoclusters on thin-film substrates with the use of femtosecond electron diffraction. Various forms of atomic motion, such as thermal vibrations, thermal expansion, and lattice disordering, manifest as distinct and quantifiable reciprocal-space observables. In photoexcited supported nanoclusters, thermal equilibration proceeds through intrinsic heat flow between their electrons and their lattice and extrinsic heat flow between the nanoclusters and their substrate. For an in-depth understanding of this process, we have extended the two-temperature model to the case of 0D/2D heterostructures and used it to describe energy flow among the various subsystems, to quantify interfacial coupling constants and to elucidate the role of the optical and thermal substrate properties. When lattice heating of Au nanoclusters is dominated by intrinsic heat flow, a reversible disordering of atomic positions occurs, which is absent when heat is injected as hot substrate phonons. The present analysis indicates that hot electrons can distort the lattice of nanoclusters, even if the lattice temperature is below the equilibrium threshold for surface premelting. Based on simple considerations, the effect is interpreted as activation of surface diffusion due to modifications of the potential energy surface at high electronic temperatures. We discuss the implications of such a process in structural changes during surface chemical reactions.

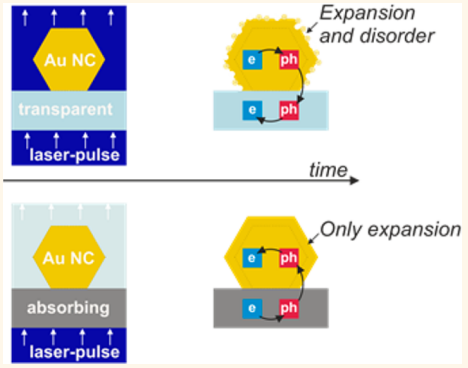

KEYWORDS: *Au nanoclusters, hot electrons, electron−lattice interactions, nanoscale heat flow, expansion, diffusion, premelting*

The most crucial achievement of nanotechnology, in line with Feynman's original vision,[1,2] is the precise arrangement of atoms to construct well-defined nanoscale building blocks. Today, the ability to synthesize metallic nanoclusters (NCs) of specific size and symmetry[3,4] and to deposit them on various surfaces with controlled density[5] offers one possibility to optimize the numerous functionalities of confined metallic systems. Recent advances in the synthesis of size-selected NCs show that the procedure can be scaled up, in order to address realistic industrial needs.[6] From the perspective of basic science, being able to prepare size-selected metallic NCs is also very promising as it allows detailed studies of their size-dependent optical,[7,8] electronic,[9] structural,[10] and catalytic[11] properties.

In all cases, it is valuable to know under which circumstances the appealing symmetry of size-selected NCs becomes fragile—a serious limitation that was raised already at the early stages of nanotechnology. Zero-dimensional metallic systems are known to have a strong tendency toward amorphization compared with their bulk analogues. For instance, the melting point of Au NCs decreases as the diameter becomes smaller.[12] In conditions close to equilibrium, the stability of NCs has been examined using electron microscopy techniques for various atomic structures[13] and temperatures,[14] whereas the nature of their equilibrium ground state has been explored using irradiation with electrons.[15] The situation is different in conditions far from equilibrium, where different subsystems of a solid can have drastically different temperatures for a very short period. Such nonequilibrium

Received: February 22, 2018
Accepted: July 11, 2018
Published: July 11, 2018

DOI: 10.1021/acsnano.8b01423
ACS Nano XXXX, XXX, XXX–XXX

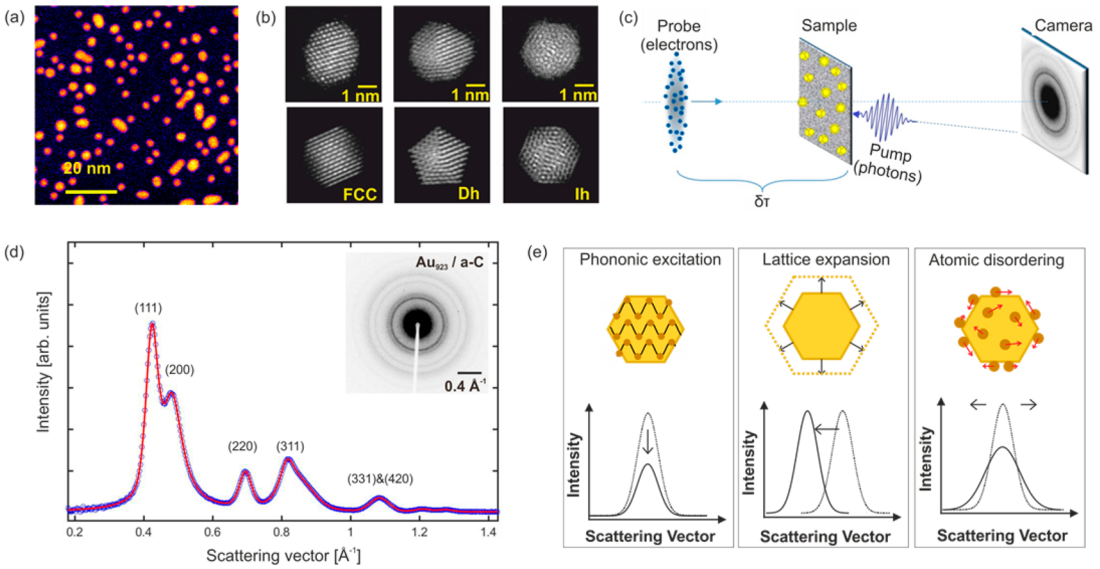

Figure 1. Electron microscopy and diffraction of size-selected Au_{923} NCs. (a) Distribution of Au_{923} NCs on the surface of a-C as observed by STEM-HAADF imaging. (b) High-resolution experimental images (top) and corresponding electron-scattering simulations (bottom) of individual NCs. (c) Schematic illustration of the FED experiment. A femtosecond laser pulse arrives at the sample at nearly normal incidence and initiates dynamics (pump). The response of the lattice is probed using short electron bunches (probe) that arrive at selected time delays ($\delta\tau$). (d) Radial average of the diffraction signal for Au_{923} NCs on a-C (blue circles) and fitting using pseudo-Voigt profiles (red line) after background subtraction. The inset shows the raw recorded diffraction pattern. (e) Observables of FED and the corresponding atomic motions in real space.

states are the key factor in numerous functionalities of metallic nanostructures, for instance, photocatalysis,[16] light-harvesting technologies,[17] or photoinduced charge transport.[18,19] To access the underlying interactions, energy flow, and transient structural properties, it is necessary to employ time-resolved techniques that are sensitive to the structural symmetry.

Ultrafast changes of the lattice order can be observed in a direct way using femtosecond diffraction.[20,21] More precisely, femtosecond electron diffraction (FED) is an appropriate investigatory tool for spatially confined systems like nanostructures and ultrathin films due to the high scattering cross-section of electrons. An in-depth understanding of the experimental results requires a realistic model of out-of-equilibrium thermodynamics. Particularly for heterostructures of low-dimensional materials, it is essential to consider not only the intrinsic properties of each component but also interactions across their interface.

In the present work, FED in combination with a model of heat flow in low-dimensional heterostructures is used to study the lattice dynamics of photoexcited, size-selected $Au_{923\pm23}$ NCs on different substrates. Au NCs and other nanostructures have been studied with time-resolved diffraction in the past in the melting and premelting regime using high incident laser fluences[22,23] as well as order−disorder dynamics of organic ligand/nanoparticle supracrystals.[24] Clark *et al.*[25] have visualized surface premelting in laser-excited Au nanocrystals composed of approximately 10^6 atoms using coherent diffraction imaging. The participation of the substrate in heat flow has been discussed in the case of Au islands and nanoparticles on graphene,[26] whereas, in a recent work, Sokolowski-Tinten *et al.* have studied heat flow in heterostructures of Au thin films and insulators.[27] Other zero-dimensional systems, examined with FED, were Bi nanoparticles[28] and quantum dots of GaAs[29] and PbSe.[30] Plech *et al.* and Hartland *et al.* observed signatures of surface melting of Au nanoparticles with optical spectroscopy.[31,32]

The experiments and modeling reported here aim to advance the field by acquiring a detailed picture of ultrafast heat flow in nanoscale heterostructures. On this basis, we demonstrate how different pathways can achieve similar maximum lattice temperatures but exhibit different time evolution and different structural changes. We study the anharmonicity and lattice expansion of Au NCs and provide experimental evidence that lattice heating by hot electrons triggers ultrafast disordering of the Au NCs' atomic lattice.

RESULTS AND DISCUSSION

The samples under investigation consist of homogeneously dispersed, size-selected clusters composed of 923 ± 23 gold atoms (from now on noted as Au_{923} for simplicity). The Au_{923} NCs are supported on thin films of 20 nm thick amorphous carbon (a-C) or 10 nm thick silicon nitride membranes (Si−N) (see Methods for details). Aberration-corrected scanning transmission electron microscopy (STEM) in high-angle annular dark-field (HAADF) mode was used to characterize the distribution of NCs, a typical image of which is shown in Figure 1a. Most NCs were identified as isolated Au_{923} (75%), whereas some aggregated and formed mostly dimers (25%). The deposited density was 8 NCs per 100 nm^2. The preparation conditions allowed, to a good extent, for adjusting the balance of the different structural allotropes.[3] In the present experiments, the amorphous-like icosahedral structures (Ih) have been nearly eliminated, and most of the NCs could be identified as decahedral (Dh) or face-centered cubic (Figure 1b). In the FED experiments depicted in Figure 1c, the samples were excited by a sub-100 fs laser pulse with a central wavelength of 400 nm, resulting in electronic excitation of the NCs and/or the substrate by optical absorption. The response of the lattice is observed by recording diffraction patterns with

DOI: 10.1021/acsnano.8b01423
ACS Nano XXXX, XXX, XXX−XXX

ultrashort electron bunches at different time delays relative to the initiating optical excitation.[33]

The recorded diffraction patterns of Au_{923} consisted of Debye–Scherrer rings, due to the random orientation of the NCs and the amorphous structure of both substrates. The diffraction patterns were radially averaged, and the diffraction intensity was plotted as a function of the scattering angle. To extract the lattice dynamics, the diffraction peaks were fitted using pseudo-Voigt peak profiles after subtraction of a background that corresponds to inelastic scattering and electrons scattered from the substrate. The selected function for the background contained the diffraction pattern of a bare substrate recorded at the same conditions, a Lorentzian function for the tail of the zero-order peak, and finally a third-order polynomial fitted in the flat regions between the various diffraction peaks (Figure S1). The result of background subtraction and fitting is shown in Figure 1d for Au_{923} on a-C, and the corresponding diffraction pattern is shown as an inset. The extracted intensities, positions, and widths of the diffraction peaks for different pump–probe delays reveal phononic excitations, lattice expansion, and atomic disordering after photoexcitation (Figure 1e).

Heat Flow Dynamics in Low-Dimensional Heterostructures. After optical excitation, the electrons thermalize within tens of femtoseconds[34] and begin to transfer heat to the lattice of Au_{923} through electron–phonon coupling. For full restoration of thermodynamic equilibrium, there should be, in addition to electron–phonon coupling, exchange of heat between the NCs and the substrate materials, through electronic or vibrational coupling. All of the above phenomena result in a time-varying energy content of the NC lattice. The accompanying structural changes become evident with changes in the intensity, position, and width of the diffraction peaks. As the lattice temperature of Au_{923} NCs increases, the intensities of the diffraction peaks decay and the background of inelastically scattered electrons increases due to the Debye–Waller effect. Furthermore, the increased lattice temperature coupled with the anharmonicity of the interatomic potential leads to thermal expansion, which becomes evident with a shift of diffraction peaks to the lower-scattering vector. This observable would be diminished in the case of thin films where lattice expansion is constrained in two dimensions. Finally, any atomic motion that leads to a deterioration of crystallinity results in peak broadening. Because of these effects, FED becomes sensitive to changes of lattice temperature and can be used to study the dynamics of nanoscale heat flow.

Previous FED experiments on bulk-like Au thin films have measured a time constant for full electron–lattice equilibration of ~4–6 ps[35,36] followed by thermal relaxation of the sample on the nanosecond to microsecond time scale. The observed dynamics of supported Au_{923} NCs are very different than bulk Au and differ markedly between the two substrates we employed. In this case, all observables have biexponential behavior at pump–probe delays shorter than 1 ns (for the underlying formulation, see Supporting Information 2). The decay of the diffraction peak intensity and the increase of the background (Debye–Waller effect) can be seen in Figure 2a for a-C and Figure 2b for Si–N supports. For a-C, the time constants are $\tau_1 = 6 \pm 2$ ps for the fast process and $\tau_2 = 80 \pm 40$ ps for the slow process. With Si–N as the substrate, the fast process has a time constant of $\tau_1 = 5.0 \pm 0.7$ ps, and the slow one, which exhibits now the reverse effect, has a time constant

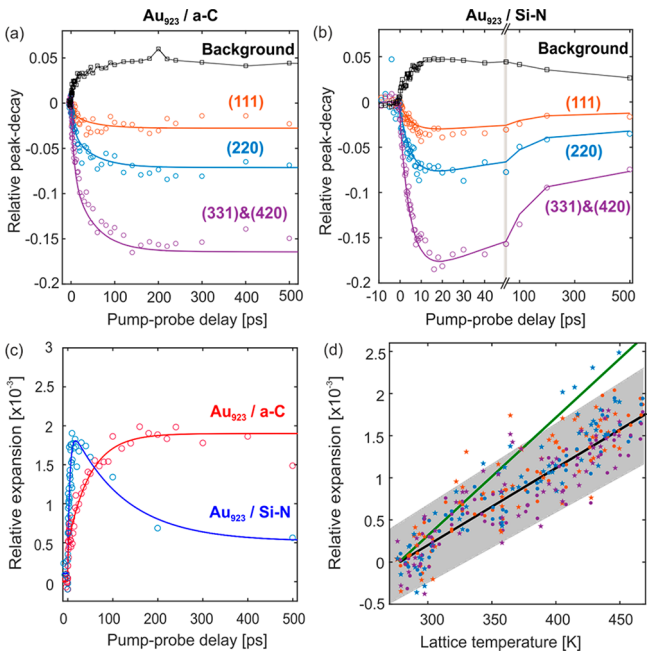

Figure 2. Laser-induced Debye–Waller effect and expansion dynamics of Au_{923}/thin-film heterostructures. (a) Peak decay and background increase as a function of pump–probe delay time for three diffraction peaks of Au_{923} on a-C (open circles) and predicted evolution based on the Debye–Waller relationship (solid lines). (b) Plot of the same quantities for Au_{923} on Si–N. (c) Relative expansion of the NCs as a function of time (open circles) and biexponential fitting (solid lines) for Au_{923} on a-C (red) and on Si–N (blue). (d) Plot of relative expansion as a function of temperature for the (111), (220), and the average of (331) and (420) peaks of Au_{923} on a-C (orange, blue, and magenta filled circles) and the average over the same peaks for Au_{923} on Si–N (same color filled stars). Each data point corresponds to a different pump–probe delay and, hence, different effective lattice temperatures. The solid black line is a linear fit that is used to extract the expansion coefficient. The gray area shows the 95% confidence intervals for a-C. Most data points of Si–N are located within these limits. The green solid line shows, for comparison, the expected slope based on the thermal expansion coefficient of bulk Au at room temperature.

of $\tau_2 = 120 \pm 50$ ps. The average thermal expansion is calculated straightforwardly from the position of diffraction peaks and is shown for both substrates in Figure 2c. The dynamics of expansion are similar to that of the Debye–Waller effect.

For both substrates, the NC coverage was the same, and so the different dynamics are due to the different optical and thermal properties of the substrate materials. In the case of a-C, both substrate and NCs are directly excited by the laser pulse. In contrast, Si–N remains largely unaffected because it is transparent at this wavelength. Thus, the equilibration with the substrate proceeds through heating of Au_{923} on a-C and cooling of Au_{923} on Si–N. Based on the lattice dynamics observed in bulk Au and the dependence of the slow process on the optical properties of the substrate, the fast process can be attributed to intrinsic electron–phonon interaction and the slow process to extrinsic coupling to the substrate, which can be used for quantitative studies of interfacial heat transport.[37] The relative amplitudes of the biexponential fitting suggest that extrinsic heating of Au_{923} NCs by heat flow from a-C contributes ~60% to the overall effect. Full thermal relaxation

DOI: 10.1021/acsnano.8b01423
ACS Nano XXXX, XXX, XXX–XXX

back to the room temperature ground state occurs on the nanosecond to microsecond time scale, that is, before the arrival of the next pump pulse, and is not investigated in this work.

To gain access into the thermodynamic properties of Au_{923} and to enable a quantitative analysis of the microscopic energy flow, it is useful to extract the atomic mean square displacement (MSD) from the peak decay using the Debye–Waller relationship:[38]

$$\frac{I_{hkl}(t)}{I_{hkl}(t<0)} = \exp\left[-\frac{4\pi^2}{3D_{hkl}^2}\left(\langle u^2\rangle_{(t)} - \langle u^2\rangle_{(t<0)}\right)\right] \quad (1)$$

This direct conversion between intensity (I_{hkl}) and MSD ($\langle u^2\rangle$) is possible because the experiments are performed in the single-scattering regime. One important detail is that it is preferable to use the total intensity and not simply the height of the diffraction peaks in the analysis because, in the latter case, possible changes of the peak profile shape are mistreated as a peak decay due to the Debye–Waller effect. The values for the interplanar spacing (D_{hkl}) in the above equation evolve with time because of the cluster expansion, as described below. With knowledge of the temperature dependence of the MSD,[39] it is now possible to extract the lattice temperature evolution as an effective measure of the time-dependent energy content of the lattice. We point out that the lattice temperature, in general, is an ill-defined quantity in strong nonequilibrium states after intense photoexcitation as different phonon modes can have different electron–phonon coupling strengths leading to nonthermal phonon distributions.[40,41] These effects can be taken into account either with the support of *ab initio* molecular dynamics[40,42] or through a momentum-resolved measurement of phonon dynamics.[41,43] Both tasks are currently unfeasible for large ensembles of randomly oriented NCs with hundreds of atoms. We therefore adopt the two-temperature approximation in the present work.

The estimated lattice temperature, plotted together with the observed relative expansion (Figure 2d), can be used to extract the thermal expansion coefficient. Within the experimental noise and the accuracy of the fitting procedure, the different peaks [(111), (220), and the average of (331) and (420)] give all the same expansion coefficient (Figure 2d). One of the basic assumptions of using the temperature dependence of MSD to estimate the lattice temperature is that lattice vibrations are harmonic. For Au_{923}, anharmonic contributions in the Debye–Waller factor do not cause significant deviations because all peaks give similar evolution of temperature and expansion.

In line with this finding, the measured thermal expansion coefficient appears to be suppressed in comparison to that with bulk Au. For the temperature range reached by ultrafast lattice heating, the average thermal expansion coefficient of Au_{923} is $a_L = (9.1 \pm 0.3) \times 10^{-6}$ K^{-1} on a-C and $a_L = (9.9 \pm 0.6) \times 10^{-6}$ K^{-1} on Si–N. For comparison, Figure 2d also contains a linear increase with a slope of 14×10^{-6} K^{-1}, which is the thermal expansion coefficient of bulk Au at room temperature.[44] Spatial confinement is thus reducing thermal expansion by ~30%. This trend has been observed in the past for similar sizes of Au NCs, using EXAFS,[45] but also for other elements such as Pt nanoparticles,[46] and it has been attributed to the large contribution of surface tension. This surface-induced compression of the Au nanolattice can cause the increased frequencies of certain vibrational modes of NCs compared to those of bulk Au.[47] To confirm that surface tension compresses Au_{923} NCs, we deposited them on few-layer graphene and recorded static diffraction patterns. By comparing the scattering vector of the (220) peak of Au (D_{220} = 1.4391 Å, for bulk Au) with the (110) peak of graphene (D_{110} = 1.2280 Å), we obtain a contraction of 0.63 ± 0.05% (Supporting Information 3). The bond-length contraction, measured with EXAFS for similar sizes,[48,49] was on the order of ~0.5–2%.

Intrinsic and Extrinsic Heat Flow in Au_{923} NCs. The dynamics of heat flow, in bulk-like metallic thin films, have been studied extensively by means of the so-called two-temperature model[50−52] (TTM). In this model, the electrons and the lattice are treated as two separate heat baths in thermal contact, each one having its own heat capacity and temperature. The incident laser pulse is expressed with a source term in the equation for the electronic temperature and the energy transfer rate from the hot electrons to the cold lattice through the electron–phonon coupling constant.

The observed substrate-dependent dynamics can be used to conceive the most basic extension of the two-temperature model in the case of low-dimensional heterostructures, a schematic illustration of which is shown in Figure 3a. This extended model contains one source term for each electronic component of the heterostructure because the substrate can also absorb light. Heat flow is then intrinsic between the electrons and the lattice of each material and extrinsic between the two different materials. Extrinsic heat flow can be carried out by transmission of hot electrons or phonons through the interface.

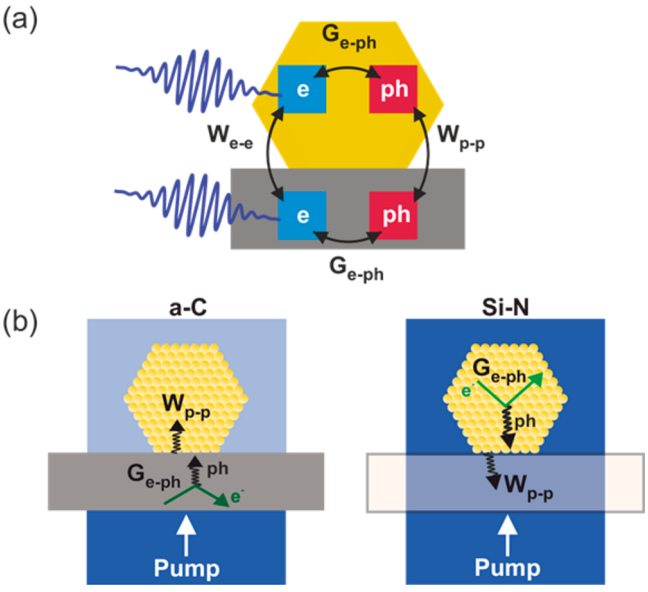

Figure 3. Schematic illustration of the model of heat flow and the observables of FED. (a) Four-temperature model for NC/thin-film heterostructures. The arrows indicate the couplings between different subsystems of the heterostructure: $G_{e\text{-}ph}$ for electron–phonon coupling within each component, $W_{e\text{-}e}$ for electronic coupling with the substrate, and $W_{p\text{-}p}$ for vibrational coupling with the substrate. (b) Different pathways for lattice heating of the NCs: extrinsic heating from the laser-excited substrate (left) and intrinsic heating through electron–phonon coupling for a transparent substrate (right).

The simple schematic of Figure 3a can be translated into four coupled differential equations that describe the time evolving energy contents of the four involved subsystems.

DOI: 10.1021/acsnano.8b01423
ACS Nano XXXX, XXX, XXX–XXX

These coupled differential equations can be used for a nonlinear fit of the experimental lattice temperature evolution and have the form

$$\frac{dT_E^{Au}}{dt} = -\frac{G_{E\text{-}PH}^{Au}}{C_E^{Au}}(T_E^{Au} - T_L^{Au}) + \frac{W_{e\text{-}e}}{L_{Au}C_E^{Au}}(T_E^{S} - T_E^{Au}) + S^{Au}(t) \quad (2)$$

$$\frac{dT_L^{Au}}{dt} = \frac{G_{E\text{-}PH}^{Au}}{C_L^{Au}}(T_E^{Au} - T_L^{Au}) + \frac{W_{p\text{-}p}}{L_{Au}C_E^{Au}}(T_L^{S} - T_L^{Au}) \quad (3)$$

$$\frac{dT_E^{S}}{dt} = -\frac{G_{E\text{-}PH}^{S}}{C_E^{S}}(T_E^{S} - T_L^{S}) - \frac{W_{e\text{-}e}}{L^{C}C_E^{S}}(T_E^{S} - T_E^{Au}) + S^{S}(t) \quad (4)$$

$$\frac{dT_L^{S}}{dt} = \frac{G_{E\text{-}PH}^{S}}{C_L^{S}}(T_E^{S} - T_L^{S}) - \frac{W_{p\text{-}p}}{L_{S}C_E^{Au}}(T_L^{S} - T_L^{Au}) \quad (5)$$

The variables T and C represent the temperature and the heat capacity of each subsystem. The upper indices denote the material (Au for Au_{923} or S for substrate), and the lower indices represent the subsystem (E for electrons and L for lattice). The electron−phonon coupling constants are denoted by $G_{e\text{-}ph}$, and the interfacial electronic and vibrational couplings are expressed by $W_{e\text{-}e}$ and $W_{p\text{-}p}$. Finally, the relative masses of the two materials are included in the equations through the effective thickness of the NC layer (L_{Au} = 1.4 nm) and the thickness of the substrate (L_S). The last terms of eqs 3 and 5 express the temporal evolution of the absorbed laser pulse and are given by

$$S(t) = \frac{F}{LC_E}\frac{\exp[-4\ln(2)(t - t_0)^2/w^2]}{w/2\sqrt{\pi/\ln(2)}} \quad (6)$$

where w is the full width at half-maximum duration of the laser pulse (w = 50 fs), F is the absorbed fluence, L is the thickness, and C_E is the electronic heat capacity of each material. The time resolution of the experimental setup is taken into account by convoluting the temperature evolutions by a Gaussian located at t_0.

The free parameters of the fitting are (i) the absorbed fluences, F_{Au} and F_S, (ii) the extrinsic coupling constants, $W_{e\text{-}e}$ and $W_{p\text{-}p}$, and (iii) the intrinsic electron−phonon coupling constant, $G_{e\text{-}ph}$, for Au_{923}. For the electron heat capacity of Au_{923}, we have used the electron heat capacity of bulk Au because electron confinement effects are expected to play a minor role for this number of atoms due to thermal broadening and screening. The lattice heat capacity of Au_{923} has been estimated by the works of Sauceda *et al.*[53,54] (see also Supporting Information 4).

In the absence of any experimental data for the electron−phonon coupling constant of a-C, its value has been selected in order to fit the reported values for the time constant of electron−lattice interactions in graphite.[55] The preparation method of the a-C thin films ensures that C atoms have an sp^2 character, and hence, the heat capacity was approximated by literature values of graphite.[56] A more detailed description of intrinsic interactions in graphitic substrates could be done, for instance, by splitting the lattice heat bath in more reservoirs, to separate the so-called strongly coupled optical phonons from all other modes.[57−59] To achieve a defined initial excitation, we have excited the sample from the side of a-C. Illumination from the side of the NCs results in an undefined distribution of the laser energy due to plasmonic enhancement of the light−matter interaction caused by the Au NCs.[60]

The fitted curves, together with the experimental evolutions of the lattice temperature, are plotted in Figure 4a for both

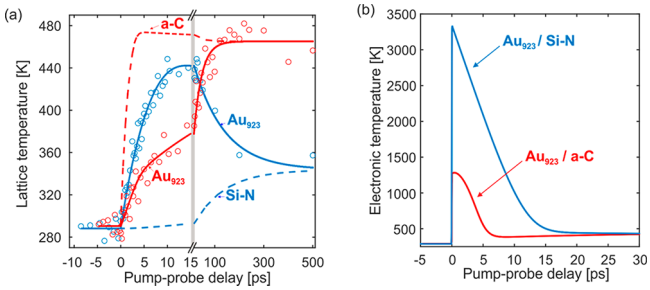

Figure 4. Evolution of electronic and lattice temperature for absorbing and transparent substrates. (a) Experimental evolution (open circles) of the Au NC lattice temperature on a-C (red) and on Si−N (blue, same color code in all subplots) and fitting based on the model of heat flow (solid lines). The predicted lattice temperature evolutions for the corresponding substrates are shown with dashed lines. (b) Prediction of the electronic temperature evolution at short time delays for both substrates (same colors). The incident fluence was ∼2.7 and ∼5.1 mJ/cm^2 for Si−N and a-C, respectively.

substrates. The maximum increase of lattice temperature is similar for both substrates (∼170 K), but the heat flow mechanism is very different. From fitting of the Au_{923} on Si−N data, we extract an electron−phonon coupling constant $G_{e\text{-}ph}^{Au}$ = (1.9 ± 0.5) × 10^{16} W/m^{3}K and a vibrational coupling constant $W_{p\text{-}p}$ = 16 ± 8 MW/m^{2}K. The data fitting reveals that the extrinsic electronic coupling $W_{e\text{-}e}$ is insignificant compared to the other coupling constants, as expected for this metal−dielectric heterostructure. To improve fit convergence, we therefore repeated the analysis with $W_{e\text{-}e}$ set to zero. The electron−phonon coupling constant extracted from four measurements is $G_{e\text{-}ph}^{Au}$ = (2 ± 0.2) × 10^{16} W/m^{3}K (Figure S4). The electron−phonon coupling constant has also been measured for free-standing thin films of Au with a thickness of 8 nm using the same apparatus, the Debye−Waller effect, and the TTM (Figure S5). The measured value is G_{bulk} = 2.7 × 10^{16} W/m^{3}K, in excellent agreement with optical pump−probe experiments analyzed with the TTM[61] that gave G_{bulk} = 2.61 × 10^{16} W/m^{3}K.

The extracted electron−phonon coupling constant of Au_{923} is ∼70% of the value of bulk Au. Recent studies have shown that in the two-temperature approximation employed here the effect of transient nonthermal phonon distributions is understimated.[40−42,62] It is thus possible that the difference in the coupling constants reflects a weakening of phonon−phonon interactions in spatially confined systems and not a genuine reduction of the electron−phonon coupling strength. The observed reduction of the thermal expansion coefficient indicates that, on average, anharmonicity is reduced in metallic NCs. It is then expected that phonon−phonon interactions will be suppressed, and the full thermalization of the lattice will be slower compared to bulk Au.

For Au_{923} on a-C, both intrinsic and extrinsic heat flow contribute to lattice heating, and the fitting becomes uncertain regarding $G_{e\text{-}ph}^{Au}$. We extract an electron−phonon coupling constant $G_{e\text{-}ph}^{Au}$ = (1.6 ± 0.9) × 10^{16} W/m^{3}K. The vibrational

DOI: 10.1021/acsnano.8b01423
ACS Nano XXXX, XXX, XXX−XXX

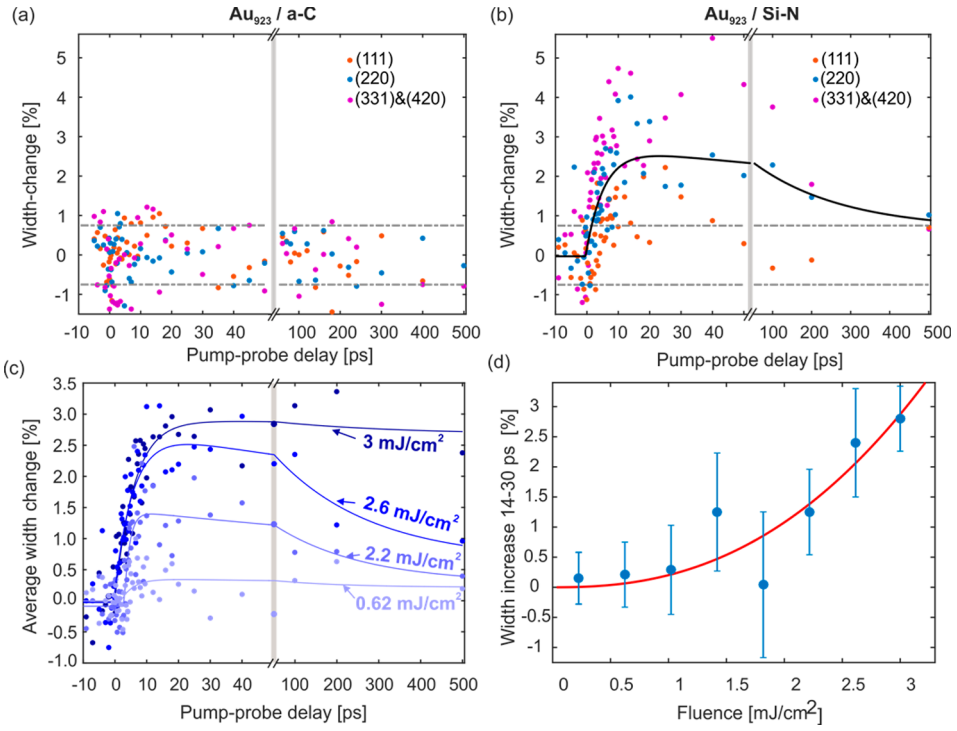

Figure 5. Ultrafast evolution and fluence dependence of diffraction peak broadening. (a) Time-dependent relative diffraction peak width (full width at half-maximum) for three Au_{923} peaks on a-C. (b) Same for Au_{923} on Si−N. The black solid line is a biexponential fit of the average width increase. (c) Average peak broadening for Au_{923} on Si−N (blue data points) and biexponential fittings (blue solid lines) for different fluences. (d) Average peak broadening as a function of the incident fluence for Au_{923} on Si−N (blue points) and error bars estimated from the standard deviation for time delays between 14 and 30 ps.

coupling constant ($W_{p\text{-}p}$) was found to be 90 ± 10 MW/m^{2}K, and the electronic coupling was smaller by a factor of 10 and thus played a minor role. The vibrational coupling to a-C is larger by a factor of 5.6 compared to that of Si−N. Besides the selection rules of interfacial phonon−phonon interactions, this quantity can also be affected by the surface morphology of the thin-film substrates. Thin films of a-C are expected to contain a variety of graphitic nanostructures and hence to have higher surface roughness and binding area.

Structural Changes Accompanying Energy Flow. Based on the model, it is now possible to compare different pathways of heat flow and elucidate their role on the observed structural changes. The starting point is the predicted evolution of the electronic temperature in the NCs. The experiment on a-C has been carried out with an incident fluence of ∼5.1 mJ/cm^2 and the experiment on Si−N with ∼2.7 mJ/cm^2. In the first case, the electrons reach a relatively small maximum temperature of ∼1300 K because the absorbing substrate depletes the incoming pulse before it arrives on the NCs. In contrast, for Au_{923} on Si−N, the maximum electronic temperature is ∼3300 K, although the incident laser fluence has been reduced.

It has been shown (Figure 2c) that the increased lattice energy content after photoexcitation is accompanied by lattice expansion and that the thermal expansion coefficient is similar for both types of substrate, although energy flows in very distinct ways. However, the evolution of the peak width shows a dependence on the substrate properties, meaning the exact pathway of energy flow. In the case of extrinsic lattice heating of the NCs through vibrational coupling to the laser excited substrate (Au_{923} on a-C), the widths of the (111), (220), (331) and (420) peaks stay constant after photoexcitation (Figure 5a). When lattice heating is carried out solely by hot electrons (Au_{923} on Si−N), the same diffraction peaks broaden after photoexcitation (Figure 5b).

The average width increase is fitted with a biexponential function shown with a black solid line in Figure 5b. The dynamics of the broadening are fast, comparable with the evolution of the lattice temperature (Figure 4a). The rise in peak width can be described with an exponential rise with a time constant of τ_1 = 5.8 ± 1.5 ps. This time constant is very similar to the time constant of the Debye−Waller dynamics (Figure 2b) or equivalently the lattice temperature increase (Figure 4a). The maximum increase of the fast process is 2.8 ± 0.4%, and subsequently, the width decreases with the time constant τ_2 ∼ 200 ps back to the ground-state value. Based on the biexponential fitting, the rise of the fast process begins upon the pulse arrival and not at later time delays when the NC lattice temperature reaches some critical value. For a better understanding of this process, the measurement of Au_{923} on Si−N has been repeated for different fluences, yielding similar time evolutions (Figure 5c). To estimate the maximum increase of width, we have averaged the experimental values from 14 to 30 ps (blue data points). The standard deviation at the same time interval has been used to estimate the corresponding error bars. The results of this procedure are plotted as a function of the estimated incident fluence in Figure 5d. The fitted function (red solid line) has the form aF^n, where F is the fluence and n = 2.4.

As illustrated in Figure 1e, an increased width of diffraction peaks is an indicator of a deterioration of crystallinity, for instance, through the formation of a noncrystalline outer shell or through the development of inhomogeneous strain. The underlying process must by nonthermal and driven by

DOI: 10.1021/acsnano.8b01423
ACS Nano XXXX, XXX, XXX−XXX

electrons; this is because (i) the peak broadening is fast and starts rising immediately after photoexcitation with a time constant similar to that of heat flow to the Au lattice; (ii) the energy content of the NCs in all measurements is below the reported threshold for initiation of surface premelting effects at this size regime[14] ($T \sim 800$ K); and (iii) the effect takes place only in the presence of hot electrons (Figure 5b) and remains unseen for slow vibrational coupling (Figure 5a). Finally, the nonlinear dependence on the incident fluence (Figure 5d) suggests that the participating atoms have to overcome an energy barrier.

Origin of Hot-Electron-Driven Peak Broadening. There are two phenomena that possibly account for the observed peak broadening: (1) activation of atomic diffusion, leading to a liquid-like layer on the surface of NCs and a reduction of the size of the crystalline core; (2) preferential coupling of electrons to collective vibrations (breathing and toroidal modes) that cause incoherent fluctuations of the NC size and shape. Breathing and toroidal modes can cause time-evolving variations on the atomic displacements across the nanostructure volume, resulting in inhomogeneous strain.[63] Coherent oscillations might not produce a coherent signal due to the NCs' size dispersion,[64] but they can give rise to an averaged peak broadening. At this size regime, the period of collective vibrations is on the order of 1 ps or lower.[8] Due to the small size of the NCs, the laser excitation will result in a homogeneous hot electron distribution within tens of femtoseconds. This is fundamentally different compared to bulk-like samples or large nanoparticles. We therefore exclude inhomogeneous electron excitation within the NCs as a cause of inhomogeneous strain[65] or structural changes induced by the hot electron blast force.[28]

We performed a size-strain analysis by comparing the broadening dynamics of two diffraction peaks[66] (see Supporting Information). The analysis of the photoinduced changes of the peak widths suggests that approximately 90% of the effect is caused by a reduction of the diameter of the crystallite, that is, by approximately 1.7%. This change in size corresponds to the removal of 50 ± 20 atoms from the crystalline core, corresponding to ∼14% of the surface atoms (for Au_{923}, the surface layer contains 362 atoms, *i.e.*, the difference with the previous magic number, Au_{561}). The measurement with the highest fluence in Figure 5c shows peak broadening for pump−probe delays up to 0.5 ns. The slow recovery of peak width is suggestive of slow recrystallization of a liquid-like surface layer, whereas collective vibrations are expected to be damped on shorter time scales due to the small size of NCs and interactions with the substrate.[8] Although inhomogeneous strain might facilitate surface disordering as discussed below, there is additional indications why strain is not the main cause for the peak broadening itself. First, the time scale of coherent acoustic vibrations (∼1 ps)[8] is distinctively faster than the observed peak broadening. Second, strain induced by coherent oscillations is expected to have a linear dependence on the vibrational amplitude and subsequently a sublinear dependence on the energy input. Thus, contributions from strain cannot account for the strongly nonlinear increase of broadening with the excitation fluence in Figure 5. Instead, the relevant lifetime, close to that of electron−phonon coupling, and the electron temperature dependence (Supporting Information section 8) suggest that the effect is triggered by hot electrons.

Our observations and considerations suggest that the dynamic diffraction peak broadening contains contribution from surface disordering of the Au NCs, which only occurs in the presence of hot electrons under pronounced electron−lattice nonequilibrium. This conclusion agrees with previous experiments. Taylor *et al.*[67] have shown that laser-irradiated Au nanorods transform into nanospheres below the melting point through diffusion of surface atoms. Clark *et al.*[25] have directly visualized the formation of such a liquid surface layer on a laser-excited Au nanoparticle using coherent diffractive X-ray imaging. In this experiment, surface disordering occurred at a temperature lower than the melting point of bulk Au, and recrystallization was slower than 500 ps.

The activation of surface diffusion of Au NCs in thermal equilibrium has been studied by *in situ* TEM measurements.[68] The range of values for the activation energy reported in that work, incorporated into the transition state theory of Eyring,[69] cannot explain the observed dynamics and the dependence of the peak broadening on the substrate material.

Our experimental findings have some similarities with the ultrafast desorption or diffusion of adsorbates on photoexcited metallic surfaces. Previous experimental[70−72] and theoretical works[73,74] have shown that hot electrons can enhance the diffusion of adsorbed molecular species on metallic surfaces due to effective excitation of adsorbate vibrations through electronic friction.[75,76] So far, self-diffusion of metal adatoms has not been taken into account in this context because the effects of electronic friction are considered less important as the atomic mass increases. However, it is known that the potential energy surface of Au changes at high electronic temperatures.[77,78] The question if hot electrons have an effect also on the surface atoms of the metal itself is largely unexplored, partially because ultrafast spectroscopic techniques do not provide direct information on the structural properties and suffer from low contrast of signatures from surface atoms compared to the bulk. Our approach of studying the structural dynamics of nanostructures with large surface-to-volume ratio with FED, however, provides sufficient sensitivity to the surface crystallinity. To explain the observed disordering of metal atoms by electronic excitations, we consider the following scenario: NCs exhibit a high density of surface states near the Fermi level, for instance, Shockley surface states or adsorbate-induced states. On Au nanofacets, surface states have been shown to be spatially inhomogeneous through scanning tunneling spectroscopy.[79] Laser excitation leads to a (de)population of electrons (below) above the Fermi level. We expect that this population redistribution results in fluctuating microscopic electric fields, both in and out of the surface plane. This process will transfer energy from the electrons to vibrations of the surface atoms, in addition to conventional electron−phonon coupling. In addition, the fluctuation in surface state occupation will result in fluctuating potential energy of the surface atoms. Through these mechanisms, surface atoms accumulate vibrational excitation and eventually get removed from their equilibrium positions. Because the proposed mechanism involves electronic surface states, the exact microscopic mechanism might depend on the facet and adsorbate coverage.

In support of this hypothesis, we note that (i) metal surfaces exhibit enhanced atomic diffusion and reconstruction when surface atoms get polarized by a static electric field,[80,81] (ii) spatially confined surface states affect the diffusion of metal adatoms on metal surfaces,[82,83] (iii) scattering by surface

DOI: 10.1021/acsnano.8b01423
ACS Nano XXXX, XXX, XXX−XXX

imperfections is a major decay channel for surface states,[84,85] and (iv) strain of metal surfaces modifies the diffusion barrier.[86] The proposed scenario has analogies to the DIMET mechanism (desorption induced by multiple electronic transitions),[87] with electronic transitions occurring between bulk and surface states, surface atoms playing the role of adsorbates, and diffusion being the resulting process instead of desorption. A final remark is that strong electric fields on the NC surface can also be created by image potential states or thermionic emission. However, these transitions have much lower probability due to their high energy.[88]

Hot Electrons in Surface Chemical Reactions. We expect our findings to be of relevance for a range of structural dynamics in nanostructures. For example, laser-excited Pd nanostructures,[89] Au/VO_2 interfaces,[90] and Au/MoS_2 heterostructures[91] have been shown to exhibit structural transformations that, in many cases, have been attributed to hot electrons. Hot electrons, however, occur not only after optical excitation with femtosecond laser pulses but also during surface chemical reactions.[92] Past studies have shown that the catalytic activity of Au NCs is accompanied by changes of their morphology,[93] more precisely sintering of the NCs, which degrades the catalytic activity. Yang *et al.*[94] have shown that during catalytically activated CO oxidation, the activation energy for sintering of Au NCs shows a 28-fold decrease. It was suggested that the detachment of surface atoms takes place due to interactions with excited electrons generated by CO oxidation. These highly excited electrons reside on surface states of the NC, which, as discussed before, can lead to surface atom diffusion.

SUMMARY

The ability to prepare 2D distributions of NCs with narrow distribution of sizes and structural allotropes, supported on various thin films, minimizes the uncertainty of structural characterization and allows FED to track the ultrafast atomic motions after photoexcitation.[22,95] We employed light-absorbing substrates (a-C) as well as transparent substrates (Si−N) to modify the pathway of ultrafast heat flow and to compare the structural changes driven by hot electrons and hot phonons. Measurements on both substrates yielded a reduced thermal expansion coefficient compared to that of bulk Au. Static measurements of Au_{923} on graphene have revealed that the lattice is compressed, even at equilibrium, due to surface tension. The next observable that has been compared between the two substrates was the peak broadening after excitation, which reflects atomic motions that reduce long-range order. This effect takes place only in the presence of hot electrons and arises from atomic disordering of the NC surfaces. We propose a mechanism leading to an enhanced excitation of surface vibrations and fluctuations of the surface potential. Our findings strongly support the general notion that hot electrons trigger surface atom diffusion in Au NCs.

The proposed mechanism of peak broadening due to surface diffusion requires that the potential energy surface is modified at high electronic temperatures. In this scenario, optical excitation with the laser pulse leads to multiple electronic transitions that involve surface states, each of them characterized by an inhomogeneous, polarizing, electric field. As a result, the potential energy surface fluctuates. Through this mechanism, surface atoms accumulate vibrational excitation and eventually get removed from their equilibrium positions. Excitation-induced strain may contribute by modulation of the surface atom diffusion barrier. Although the exact mechanism is still to be verified, the possibility that electronic excitations facilitate surface diffusion can be an essential part of the morphological changes of NCs induced by surface chemical reactions or laser irradiation.

METHODS

Size-Selected Synthesis. Size-selected Au nanoclusters were produced using a magnetron sputtering gas aggregation cluster source[4] with a lateral time-of-flight mass filter.[96] A mass resolution of $M/\Delta M = 20$ was applied to give clusters with 923 ± 23 atoms. The clusters were deposited on either copper TEM grids coated with a thin film of a-C (20 nm thick), silicon TEM grids with an array of Si−N windows (100 μm wide and 10 nm thick), and few-layer graphene (used as a reference material to investigate static lattice compression due to surface tension). The Au_{923} NCs were deposited in the "soft-landing" regime (<2 eV/atom) to prevent fragmentation and maintain the cluster structure.[5] The deposition density was eight clusters per 100 nm^2, and all formation conditions were kept the same so as not to change the relative proportions of structural isomers.[3] To immobilize the clusters, defects were created prior to cluster deposition by exposure of the substrate to a high energy Ar+ beam (1500 V).

After deposition, the samples on conducting substrates were examined using a 200 keV JEOL JEM 2100F STEM with a spherical aberration corrector (CEOS). A HAADF detector with inner collection angle of 62 mrad was employed for *z*-contrast imaging of the samples; in this mode, the intensity is linearly proportional to the number of atoms.[97] This enabled the 3D atomic structure of the clusters to be determined[97] and for the size distribution to be calculated using the size-selected Au_{923} clusters as a mass balance.[98]

FED Experiments. Time-resolved measurements have been carried out with FED operated with a repetition rate of 1 kHz. Individual electron bunches contained a few thousand electrons. The diffractometer is characterized by a highly compact design, and the transverse coherence of the electron beam is larger than the diameter of the Au NCs under investigation.[33] For each time delay, 40000 diffraction patterns were integrated for Au_{923} on a-C and 20000−40000 for the fluence dependence measurements on Si−N. The acceleration voltage of the electrons was kept at 93 keV, and the estimated time resolution was on the order of ∼300 fs. The substrate's contribution to the diffraction patterns was taken into account by recording the diffraction pattern of a bare substrate under the same experimental conditions.

ASSOCIATED CONTENT

Supporting Information

The Supporting Information is available free of charge on the ACS Publications website at DOI: 10.1021/acsnano.8b01423.

Illustration of the background subtraction before fitting the time-resolved diffraction patterns; static measurements of Au NCs on graphene to extract lattice compression at equilibrium; additional measurements of the electron−phonon coupling constant for Au_{923} on Si−N; measurement of the electron−phonon coupling constant for bulk-like, free-standing, Au films; peak broadening as a function of the maximum electronic temperature; discussion on the effect of photoinduced charging at higher laser fluences and its effect on the FED measurements; test measurement at different sample and experimental conditions; additional analysis of the anharmonicity of Au_{923} NCs; and fluence dependence measurements of peak broadening for Au_{923} on a-C (PDF)

DOI: 10.1021/acsnano.8b01423
ACS Nano XXXX, XXX, XXX−XXX

AUTHOR INFORMATION

Corresponding Authors

*E-mail: vasileiadis@fhi-berlin.mpg.de.
*E-mail: ernstorfer@fhi-berlin.mpg.de.

ORCID

Lutz Waldecker: 0000-0002-0898-3860
Richard E. Palmer: 0000-0001-8728-8083
Ralph Ernstorfer: 0000-0001-6665-3520

Present Addresses

[‖]Department of Applied Physics, Stanford University, Stanford, CA 94305, USA.
[⊥]Institut de Physique de Rennes, University of Rennes, UMR UR1-CNRS 6251, F-35000 Rennes, France.

Notes

The authors declare no competing financial interest.

ACKNOWLEDGMENTS

We thank Alexander Paarmann, Alexey Melnikov, Martin Wolf, and Peter Saalfrank for useful comments and discussions. This project has received funding from the Max Planck Society and from the European Research Council (ERC) under the European Union's Horizon 2020 research and innovation program (Grant Agreement Number ERC-2015-CoG-682843). R.B. acknowledges funding from the Alexander von Humboldt Foundation and A.S. from the Brazilian National Council of Technological and Scientific Development (CNPq).

REFERENCES

(1) Feynman, R. P. There's Plenty of Room at the Bottom. *J. Microelectromech. Syst.* **1992**, *1*, 60−66.
(2) Feynman, R. P. Infinitesimal Machinery. *J. Microelectromech. Syst.* **1993**, *2*, 4−14.
(3) Plant, S. R.; Cao, L.; Palmer, R. E. Atomic Structure Control of Size-Selected Gold Nanoclusters during Formation. *J. Am. Chem. Soc.* **2014**, *136*, 7559−7562.
(4) Pratontep, S.; Carroll, S. J.; Xirouchaki, C.; Streun, M.; Palmer, R. E. Size-Selected Cluster Beam Source Based on Radio Frequency Magnetron Plasma Sputtering and Gas Condensation. *Rev. Sci. Instrum.* **2005**, *76*, 045103.
(5) Di Vece, M.; Palomba, S.; Palmer, R. E. Pinning of Size-Selected Gold and Nickel Nanoclusters on Graphite. *Phys. Rev. B: Condens. Matter Mater. Phys.* **2005**, *72*, 073407.
(6) Palmer, R. E.; Cao, L.; Yin, F. Note: Proof of Principle of a New Type of Cluster Beam Source with Potential for Scale-Up. *Rev. Sci. Instrum.* **2016**, *87*, 046103.
(7) Zheng, J.; Nicovich, P. R.; Dickson, R. M. Highly Fluorescent Noble-Metal Quantum Dots. *Annu. Rev. Phys. Chem.* **2007**, *58*, 409−431.
(8) Yau, S. H.; Varnavski, O.; Goodson, T. An Ultrafast Look at Cluster Dynamics. *Acc. Chem. Res.* **2013**, *46*, 1506−1516.
(9) Walter, M.; Akola, J.; Lopez-Acevedo, O.; Jadzinsky, P. D.; Calero, G.; Ackerson, C. J.; Whetten, R. L.; Grönbeck, H.; Häkkinen, H. A Unified View of Ligand-Protected Gold Clusters as Superatom Complexes. *Proc. Natl. Acad. Sci. U. S. A.* **2008**, *105*, 9157−9162.
(10) Baletto, F.; Ferrando, R. Structural Properties of Nanoclusters: Energetic, Thermodynamic, and Kinetic Effects. *Rev. Mod. Phys.* **2005**, *77*, 371.
(11) Tyo, E. C.; Vajda, S. Catalysis by Clusters with Precise Numbers of Atoms. *Nat. Nanotechnol.* **2015**, *10*, 577−588.
(12) Buffat, P.; Borel, J.-P. Size Effect on the Melting Temperature of Gold Particles. *Phys. Rev. A: At., Mol., Opt. Phys.* **1976**, *13*, 2287−2298.
(13) Wells, D. M.; Rossi, G.; Ferrando, R.; Palmer, R. E. Metastability of the Atomic Structures of Size-Selected Gold Nanoparticles. *Nanoscale* **2015**, *7*, 6498−6503.
(14) Barnard, A. S.; Young, N. P.; Kirkland, A. I.; Van Huis, M. A.; Xu, H. Nanogold: A Quantitative Phase Map. *ACS Nano* **2009**, *3*, 1431−1436.
(15) Wang, Z. W.; Palmer, R. E. Determination of the Ground-State Atomic Structures of Size-Selected Au Nanoclusters by Electron-Beam-Induced Transformation. *Phys. Rev. Lett.* **2012**, *108*, 245502.
(16) Mukherjee, S.; Libisch, F.; Large, N.; Neumann, O.; Brown, L. V.; Cheng, J.; Lassiter, J. B.; Carter, E. A.; Nordlander, P.; Halas, N. J. Hot Electrons Do the Impossible: Plasmon-Induced Dissociation of H_2 on Au. *Nano Lett.* **2013**, *13*, 240−247.
(17) Fang, Z.; Liu, Z.; Wang, Y.; Ajayan, P. M.; Nordlander, P.; Halas, N. J. Graphene-Antenna Sandwich Photodetector. *Nano Lett.* **2012**, *12*, 3808−3813.
(18) Brongersma, M. L.; Halas, N. J.; Nordlander, P. Plasmon-Induced Hot Carrier Science and Technology. *Nat. Nanotechnol.* **2015**, *10*, 25−34.
(19) Kumar, D.; Lee, A.; Lee, T.; Lim, M.; Lim, D. K. Ultrafast and Efficient Transport of Hot Plasmonic Electrons by Graphene for Pt Free, Highly Efficient Visible-Light Responsive Photocatalyst. *Nano Lett.* **2016**, *16*, 1760−1767.
(20) Dwyer, J. R.; Hebeisen, C. T.; Ernstorfer, R.; Harb, M.; Deyirmenjian, V. B.; Jordan, R. E.; Miller, R. J. D. Femtosecond Electron Diffraction: 'Making the Molecular Movie'. *Philos. Trans. R. Soc., A* **2006**, *364*, 741−778.
(21) Miller, R. J. D.; Ernstorfer, R.; Harb, M.; Gao, M.; Hebeisen, C. T.; Jean-Ruel, H.; Lu, C.; Moriena, G.; Sciaini, G. 'Making the Molecular Movie': First Frames. *Acta Crystallogr., Sect. A: Found. Crystallogr.* **2010**, *66*, 137−156.
(22) Ruan, C. Y.; Murooka, Y.; Raman, R. K.; Murdick, R. A. Dynamics of Size-Selected Gold Nanoparticles Studied by Ultrafast Electron Nanocrystallography. *Nano Lett.* **2007**, *7*, 1290−1296.
(23) Plech, A.; Kotaidis, V.; Grésillon, S.; Dahmen, C.; Von Plessen, G. Laser-Induced Heating and Melting of Gold Nanoparticles Studied by Time-Resolved X-Ray Scattering. *Phys. Rev. B: Condens. Matter Mater. Phys.* **2004**, *70*, 195423.
(24) Mancini, G. F.; Latychevskaia, T.; Pennacchio, F.; Reguera, J.; Stellacci, F.; Carbone, F. Order/Disorder Dynamics in a Dodecanethiol-Capped Gold Nanoparticles Supracrystal by Small-Angle Ultrafast Electron Diffraction. *Nano Lett.* **2016**, *16*, 2705−2713.
(25) Clark, J. N.; Beitra, L.; Xiong, G.; Fritz, D. M.; Lemke, H. T.; Zhu, D.; Chollet, M.; Williams, G. J.; Messerschmidt, M. M.; Abbey, B.; Harder, R. J.; Korsunsky, A. M.; Wark, J. S.; Reis, D. A.; Robinson, I. K. Imaging Transient Melting of a Nanocrystal Using an X-ray Laser. *Proc. Natl. Acad. Sci. U. S. A.* **2015**, *112*, 7444−7448.
(26) Liang, W.; Schäfer, S.; Zewail, A. H. Ultrafast Electron Crystallography of Heterogeneous Structures: Gold-Graphene Bilayer and Ligand-Encapsulated Nanogold on Graphene. *Chem. Phys. Lett.* **2012**, *542*, 8−12.
(27) Sokolowski-Tinten, K.; Shen, X.; Zheng, Q.; Chase, T.; Coffee, R.; Jerman, M.; Li, R. K.; Ligges, M.; Makasyuk, I.; Mo, M.; Reid, A. H.; Rethfeld, B.; Vecchione, T.; Weathersby, S. P.; Dürr, H. A.; Wang, X. J. Electron-Lattice Energy Relaxation in Laser-Excited Thin-Film Au-Insulator Heterostructures Studied by Ultrafast MeV Electron Diffraction. *Struct. Dyn.* **2017**, *4*, 054501.
(28) Esmail, A. R.; Bugayev, A.; Elsayed-Ali, H. E. Electron Diffraction Studies of Structural Dynamics of Bismuth Nanoparticles. *J. Phys. Chem. C* **2013**, *117*, 9035−9041.
(29) Vanacore, G. M.; Hu, J.; Liang, W.; Bietti, S.; Sanguinetti, S.; Zewail, A. H. Diffraction of Quantum Dots Reveals Nanoscale Ultrafast Energy Localization. *Nano Lett.* **2014**, *14*, 6148−6154.
(30) Wang, X.; Rahmani, H.; Zhou, J.; Gorfien, M.; Plaskus, J. M.; Li, D.; Voss, R.; Nelson, C. A.; Lei, K. W.; Wolcott, A.; Zhu, X.; Li, J.; Cao, J. Ultrafast Lattice Dynamics in Lead Selenide Quantum Dot Induced by Laser Excitation. *Appl. Phys. Lett.* **2016**, *109*, 153105.

DOI: 10.1021/acsnano.8b01423
ACS Nano XXXX, XXX, XXX−XXX

(31) Plech, A.; Cerna, R.; Kotaidis, V.; Hudert, F.; Bartels, A.; Dekorsy, T. A Surface Phase Transition of Supported Gold Nanoparticles. *Nano Lett.* **2007**, *7*, 1026−1031.
(32) Hartland, G. V.; Hu, M.; Sader, J. E. Softening of the Symmetric Breathing Mode in Gold Particles by Laser-Induced Heating. *J. Phys. Chem. B* **2003**, *107*, 7472−7478.
(33) Waldecker, L.; Bertoni, R.; Ernstorfer, R. Compact Femtosecond Electron Diffractometer with 100 keV Electron Bunches Approaching the Single-Electron Pulse Duration Limit. *J. Appl. Phys.* **2015**, *117*, 044903.
(34) Saavedra, J. R. M.; Asenjo-Garcia, A.; García de Abajo, F. J. Hot-Electron Dynamics and Thermalization in Small Metallic Nanoparticles. *ACS Photonics* **2016**, *3*, 1637−1646.
(35) Ligges, M.; Rajković, I.; Streubühr, C.; Brazda, T.; Zhou, P.; Posth, O.; Hassel, C.; Dumpich, G.; Von der Linde, D. Transient (000)-Order Attenuation Effects in Ultrafast Transmission Electron Diffraction. *J. Appl. Phys.* **2011**, *109*, 063519.
(36) White, T. G.; Mabey, P.; Gericke, D. O.; Hartley, N. J.; Doyle, H. W.; McGonegle, D.; Rackstraw, D. S.; Higginbotham, A.; Gregori, G. Electron-Phonon Equilibration in Laser-Heated Gold Films. *Phys. Rev. B: Condens. Matter Mater. Phys.* **2014**, *90*, 014305.
(37) Witte, T.; Frigge, T.; Hafke, B.; Krenzer, B.; Horn-von Hoegen, M. Nanoscale Interfacial Heat Transport of Ultrathin Epitaxial Hetero Films: Few Monolayer Pb (111) on Si (111). *Appl. Phys. Lett.* **2017**, *110*, 243103.
(38) Peng, L. M.; Dudarev, S. L.; Whelan, M. J. *High-Energy Electron Diffraction and Microscopy*; Oxford Science Publications, 2004.
(39) Solliard, C. Debye-Waller Factor and Melting Temperature in Small Gold Particles: Related Size Effects. *Solid State Commun.* **1984**, *51*, 947−949.
(40) Waldecker, L.; Bertoni, R.; Ernstorfer, R.; Vorberger, J. Electron-Phonon Coupling and Energy Flow in a Simple Metal beyond the Two-Temperature Approximation. *Phys. Rev. X* **2016**, *6*, 021003.
(41) Chase, T.; Trigo, M.; Reid, A. H.; Li, R.; Vecchione, T.; Shen, X.; Weathersby, S.; Coffee, R.; Hartmann, N.; Reis, D. A.; Wang, X. J.; Dürr, H. A. Ultrafast Electron Diffraction from Non-Equilibrium Phonons in Femtosecond Laser Heated Au Films. *Appl. Phys. Lett.* **2016**, *108*, 041909.
(42) Waldecker, L.; Vasileiadis, T.; Bertoni, R.; Ernstorfer, R.; Zier, T.; Valencia, F. H.; Garcia, M. E.; Zijlstra, E. S. Coherent and Incoherent Structural Dynamics in Laser-Excited Antimony. *Phys. Rev. B: Condens. Matter Mater. Phys.* **2017**, *95*, 054302.
(43) Waldecker, L.; Bertoni, R.; Hübener, H.; Brumme, T.; Vasileiadis, T.; Zahn, D.; Rubio, A.; Ernstorfer, R. Momentum-Resolved View of Electron-Phonon Coupling in Multilayer WSe_2. *Phys. Rev. Lett.* **2017**, *119*, 036803.
(44) Nix, F. C.; MacNair, D. The Thermal Expansion of Pure Metals: Copper, Gold, Aluminum, Nickel, and Iron. *Phys. Rev.* **1941**, *60*, 597.
(45) Comaschi, T.; Balerna, A.; Mobilio, S. Temperature Dependence of the Structural Parameters of Gold Nanoparticles Investigated with EXAFS. *Phys. Rev. B: Condens. Matter Mater. Phys.* **2008**, *77*, 075432.
(46) Roldan Cuenya, B.; Frenkel, A. I.; Mostafa, S.; Behafarid, F.; Croy, J. R.; Ono, L. K.; Wang, Q. Anomalous Lattice Dynamics and Thermal Properties of Supported Size- and Shape-Selected Pt Nanoparticles. *Phys. Rev. B: Condens. Matter Mater. Phys.* **2010**, *82*, 155450.
(47) Bayle, M.; Combe, N.; Sangeetha, N. M.; Viau, G.; Carles, R. Vibrational and Electronic Excitations in Gold Nanocrystals. *Nanoscale* **2014**, *6*, 9157−9165.
(48) Pinto, A.; Pennisi, A. R.; Faraci, G.; D'Agostino, G.; Mobilio, S.; Boscherini, F. Evidence for Truncated Octahedral Structures in Supported Gold Clusters. *Phys. Rev. B: Condens. Matter Mater. Phys.* **1995**, *51*, 5315−5321.
(49) Miller, J. T.; Kropf, A. J.; Zha, Y.; Regalbuto, J. R.; Delannoy, L.; Louis, C.; Bus, E.; Van Bokhoven, J. A. The Effect of Gold Particle Size on Au-Au Bond Length and Reactivity toward Oxygen in Supported Catalysts. *J. Catal.* **2006**, *240*, 222−234.
(50) Anisimov, S. I.; Bonch-Bruevich, A. M.; Elyashevich, M. A.; Imas, Y. A.; Pavlenko, N. A.; Romanov, G. S. Effect of Powerful Light Fluxes on Metals. *Sov. Phys. Technol. Phys.* **1967**, *11*, 945.
(51) Allen, P. B. Theory of Thermal Relaxation of Electrons in Metals. *Phys. Rev. Lett.* **1987**, *59*, 1460.
(52) Lin, Z.; Zhigilei, L. V.; Celli, V. Electron-Phonon Coupling and Electron Heat Capacity of Metals under Conditions of Strong Electron-Phonon Nonequilibrium. *Phys. Rev. B: Condens. Matter Mater. Phys.* **2008**, *77*, 075133.
(53) Sauceda, H. E.; Salazar, F.; Pérez, L. A.; Garzón, I. L. Size and Shape Dependence of the Vibrational Spectrum and Low-Temperature Specific Heat of Au Nanoparticles. *J. Phys. Chem. C* **2013**, *117*, 25160−25168.
(54) Sauceda, H. E.; Mongin, D.; Maioli, P.; Crut, A.; Pellarin, M.; Del Fatti, N.; Vallée, F.; Garzón, I. L. Vibrational Properties of Metal Nanoparticles: Atomistic Simulation and Comparison with Time-Resolved Investigation. *J. Phys. Chem. C* **2012**, *116*, 25147−25156.
(55) Carbone, F.; Aubock, G.; Cannizzo, A.; Van Mourik, F.; Nair, R. R.; Geim, A. K.; Novoselov, K. S.; Chergui, M. Femtosecond Carrier Dynamics in Bulk Graphite and Graphene Paper. *Chem. Phys. Lett.* **2011**, *504*, 37−40.
(56) Pop, E.; Varshney, V.; Roy, A. K. Thermal Properties of Graphene: Fundamentals and Applications. *MRS Bull.* **2012**, *37*, 1273−1281.
(57) Lui, C. H.; Mak, K. F.; Shan, J.; Heinz, T. F. Ultrafast Photoluminescence from Graphene. *Phys. Rev. Lett.* **2010**, *105*, 127404.
(58) Chatelain, R. P.; Morrison, V. R.; Klarenaar, B. L. M.; Siwick, B. J. Coherent and Incoherent Electron-Phonon Coupling in Graphite Observed with Radio-Frequency Compressed Ultrafast Electron Diffraction. *Phys. Rev. Lett.* **2014**, *113*, 235502.
(59) Harb, M.; Enquist, H.; Jurgilaitis, A.; Tuyakova, F. T.; Obraztsov, A. N.; Larsson, J. Phonon-Phonon Interactions in Photoexcited Graphite Studied by Ultrafast Electron Diffraction. *Phys. Rev. B: Condens. Matter Mater. Phys.* **2016**, *93*, 104104.
(60) Du, Y.; Zhao, Y.; Qu, Y.; Chen, C.-H.; Chen, C.-M.; Chuang, C.-H.; Zhu, Y. Enhanced Light-Matter Interaction of Graphene-Gold Nanoparticle Hybrid Films for High-Performance SERS Detection. *J. Mater. Chem. C* **2014**, *2*, 4683.
(61) Brorson, S. D.; Kazeroonian, A.; Moodera, J. S.; Face, D. W.; Cheng, T. K.; Ippen, E. P.; Dresselhaus, M. S.; Dresselhaus, G. Femtosecond Room-Temperature Measurement of the Electron-Phonon Coupling Constant λ in Metallic Superconductors. *Phys. Rev. Lett.* **1990**, *64*, 2172.
(62) Ono, S. Thermalization in Simple Metals: Role of Electron-Phonon and Phonon-Phonon Scattering. *Phys. Rev. B: Condens. Matter Mater. Phys.* **2018**, *97*, 054310.
(63) Plech, A.; Grésillon, S.; Von Plessen, G.; Scheidt, K.; Naylor, G. Structural Kinetics of Laser-Excited Metal Nanoparticles Supported on a Surface. *Chem. Phys.* **2004**, *299*, 183−191.
(64) Van Dijk, M. A.; Lippitz, M.; Orrit, M. Detection of Acoustic Oscillations of Single Gold Nanospheres by Time-Resolved Interferometry. *Phys. Rev. Lett.* **2005**, *95*, 267406.
(65) Reis, D. A.; DeCamp, M. F.; Bucksbaum, P. H.; Clarke, R.; Dufresne, E.; Hertlein, M.; Merlin, R.; Falcone, R.; Kapteyn, H.; Murnane, M. M.; Larsson, J.; Missalla, Th.; Wark, J. S. Probing Impulsive Strain Propagation with X-Ray Pulses. *Phys. Rev. Lett.* **2001**, *86*, 3072.
(66) Williamson, G. K.; Hall, W. H. X-ray Line Broadening from Filed Aluminium and Wolfram. *Acta Metall.* **1953**, *1*, 22−31.
(67) Taylor, A. B.; Siddiquee, A. M.; Chon, J. W. M. Below Melting Point Photothermal Reshaping of Single Gold Nanorods Driven by Surface Diffusion. *ACS Nano* **2014**, *8*, 12071−12079.
(68) Surrey, A.; Pohl, D.; Schultz, L.; Rellinghaus, B. Quantitative Measurement of the Surface Self-Diffusion on Au Nanoparticles by Aberration-Corrected Transmission Electron Microscopy. *Nano Lett.* **2012**, *12*, 6071−6077.

DOI: 10.1021/acsnano.8b01423
ACS Nano XXXX, XXX, XXX−XXX

(69) Eyring, H. The Activated Complex in Chemical Reactions. *J. Chem. Phys.* **1935**, *3*, 107−115.
(70) Stépán, K.; Dürr, M.; Güdde, J.; Höfer, U. Laser-Induced Diffusion of Oxygen on a Stepped Pt (111) Surface. *Surf. Sci.* **2005**, *593*, 54−66.
(71) Lawrenz, M.; Stépán, K.; Güdde, J.; Höfer, U. Time-Domain Investigation of Laser-Induced Diffusion of CO on a Vicinal Pt (111) Surface. *Phys. Rev. B: Condens. Matter Mater. Phys.* **2009**, *80*, 075429.
(72) Mehlhorn, M.; Gawronski, H.; Morgenstern, K. Diffusion and Dimer Formation of CO Molecules Induced by Femtosecond Laser Pulses. *Phys. Rev. Lett.* **2010**, *104*, 076101.
(73) Ueba, H.; Ootsuka, Y.; Paulsson, M.; Persson, B. N. J. Lateral Hopping of CO on Cu(111) Induced by Femtosecond Laser Pulses. *Phys. Rev. B: Condens. Matter Mater. Phys.* **2010**, *82*, 121411.
(74) Scholz, R.; Floß, G.; Saalfrank, P.; Füchsel, G.; Lončarić, I.; Juaristi, J. I. Femtosecond-Laser Induced Dynamics of CO on Ru (0001): Deep Insights from a Hot-Electron Friction Model Including Surface Motion. *Phys. Rev. B: Condens. Matter Mater. Phys.* **2016**, *94*, 165447.
(75) Frischkorn, C.; Wolf, M. Femtochemistry at Metal Surfaces: Nonadiabatic Reaction Dynamics. *Chem. Rev.* **2006**, *106*, 4207−4233.
(76) Brandbyge, M.; Hedegård, P.; Heinz, T. F.; Misewich, J. A.; Newns, D. M. Electronically Driven Adsorbate Excitation Mechanism in Femtosecond-Pulse Laser Desorption. *Phys. Rev. B: Condens. Matter Mater. Phys.* **1995**, *52*, 6042−6056.
(77) Bottin, F.; Zérah, G. Formation Enthalpies of Monovacancies in Aluminum and Gold under the Condition of Intense Laser Irradiation. *Phys. Rev. B: Condens. Matter Mater. Phys.* **2007**, *75*, 174114.
(78) Ernstorfer, R.; Harb, M.; Hebeisen, C. T.; Sciaini, G.; Dartigalongue, T.; Miller, R. J. D. The Formation of Warm Dense Matter: Experimental Evidence for Electronic Bond Hardening in Gold. *Science* **2009**, *323*, 1033−1037.
(79) Barke, I.; Hövel, H. Confined Shockley Surface States on the (111) Facets of Gold Clusters. *Phys. Rev. Lett.* **2003**, *90*, 166801.
(80) Olsen, M.; Hummelgård, M.; Olin, H. Surface Modifications by Field Induced Diffusion. *PLoS One* **2012**, *7*, e30106.
(81) Simic-Milosevic, V.; Heyde, M.; Nilius, N.; Nowicki, M.; Rust, H.-P.; Freund, H.-J. Substrate-Mediated Interaction and Electron-Induced Diffusion of Single Lithium Atoms on Ag(001). *Phys. Rev. B: Condens. Matter Mater. Phys.* **2007**, *75*, 195416.
(82) Negulyaev, N. N.; Stepanyuk, V. S.; Niebergall, L.; Bruno, P.; Hergert, W.; Repp, J.; Rieder, K.-H.; Meyer, G. Direct Evidence for the Effect of Quantum Confinement of Surface-State Electrons on Atomic Diffusion. *Phys. Rev. Lett.* **2008**, *101*, 226601.
(83) Ternes, M.; Pivetta, M.; Patthey, F.; Schneider, W.-D. Creation, Electronic Properties, Disorder, and Melting of Two-Dimensional Surface-State-Mediated Adatom Superlattices. *Prog. Surf. Sci.* **2010**, *85*, 1−27.
(84) Kliewer, J.; Berndt, R.; Chulkov, E. V.; Silkin, V. M.; Echenique, P. M.; Crampin, S. Dimensionality Effects in the Lifetime of Surface States. *Science* **2000**, *288*, 1399−1402.
(85) Sklyadneva, I. Yu.; Heid, R.; Silkin, V. M.; Melzer, A.; Bohnen, K. P.; Echenique, P. M.; Fauster, Th.; Chulkov, E. V. Unusually Weak Electron-Phonon Coupling in the Shockley Suface State on Pd(111). *Phys. Rev. B: Condens. Matter Mater. Phys.* **2009**, *80*, 045429.
(86) Brune, H.; Bromann, K.; Röder, H.; Kern, K.; Jacobsen, J.; Stoltze, P.; Jacobsen, K.; Nørskov, J. Effect of Strain on Surface Diffusion and Nucleation. *Phys. Rev. B: Condens. Matter Mater. Phys.* **1995**, *52*, R14380.
(87) Misewich, J. A.; Heinz, T. F.; Newns, D. M. Desorption Induced by Multiple Electronic Transitions. *Phys. Rev. Lett.* **1992**, *68*, 3737.
(88) Höfer, U.; Shumay, I. L.; Reuß, Ch.; Thomann, U.; Wallauer, W.; Fauster, Th. Time-Resolved Coherent Photoelectron Spectroscopy of Quantized Electronic States on Metal Surfaces. *Science* **1997**, *277*, 1480−1482.
(89) Wille, A.; Buchwald, R.; Al-Shamery, K. Adsorbate-Induced Roughening of Nanosized Palladium Particles after Coherent Laser Excitation. *Appl. Phys. A: Mater. Sci. Process.* **2004**, *78*, 205−211.
(90) Appavoo, K.; Wang, B.; Brady, N. F.; Seo, M.; Nag, J.; Prasankumar, R. P.; Hilton, D. J.; Pantelides, S. T.; Haglund, R. F. Ultrafast Phase Transition *via* Catastrophic Phonon Collapse Driven by Plasmonic Hot-Electron Injection. *Nano Lett.* **2014**, *14*, 1127−1133.
(91) Kang, Y.; Najmaei, S.; Liu, Z.; Bao, Y.; Wang, Y.; Zhu, X.; Halas, N. J.; Nordlander, P.; Ajayan, P. M.; Lou, J.; Fang, Z. Plasmonic Hot Electron Induced Structural Phase Transition in a MoS_2 Monolayer. *Adv. Mater.* **2014**, *26*, 6467−6471.
(92) Park, J. Y.; Kim, S. M.; Lee, H.; Nedrygailov, I. I. Hot-Electron-Mediated Surface Chemistry : Toward Electronic Control of Catalytic Activity. *Acc. Chem. Res.* **2015**, *48*, 2475−2483.
(93) Laoufi, I.; Saint-Lager, M.-C.; Lazzari, R.; Jupille, J.; Robach, O.; Garaudée, S.; Cabailh, G.; Dolle, P.; Cruguel, H.; Bailly, A. Size and Catalytic Activity of Supported Gold Nanoparticles: An in Operando Study during CO Oxidation. *J. Phys. Chem. C* **2011**, *115*, 4673−4679.
(94) Yang, F.; Chen, M. S.; Goodman, D. W. Sintering of Au Particles Supported on TiO_2 (110) during CO Oxidation. *J. Phys. Chem. C* **2009**, *113*, 254−260.
(95) Ruan, C.-Y.; Murooka, Y.; Raman, R. K.; Murdick, R. A.; Worhatch, R. J.; Pell, A. The Development and Applications of Ultrafast Electron Nanocrystallography. *Microsc. Microanal.* **2009**, *15*, 323−337.
(96) Von Issendorff, B.; Palmer, R. E. A New High Transmission Infinite Range Mass Selector for Cluster and Nanoparticle Beams. *Rev. Sci. Instrum.* **1999**, *70*, 4497.
(97) Li, Z. Y.; Young, N. P.; Di Vece, M.; Palomba, S.; Palmer, R. E.; Bleloch, A. L.; Curley, B. C.; Johnston, R. L.; Jiang, J.; Yuan, J. Three-Dimensional Atomic-Scale Structure of Size-Selected Gold Nanoclusters. *Nature* **2008**, *451*, 46−48.
(98) Young, N. P.; Li, Z. Y.; Chen, Y.; Palomba, S.; Di Vece, M.; Palmer, R. E. Weighing Supported Nanoparticles: Size-Selected Clusters as Mass Standards in Nanometrology. *Phys. Rev. Lett.* **2008**, *101*, 246103.

DOI: 10.1021/acsnano.8b01423
ACS Nano XXXX, XXX, XXX−XXX